A class of topological nodal rings and its realization in carbon networks

Yan Gao, Yuanping Chen, Yuee Xie, Po-Yao Chang, Marvin L. Cohen, and Shengbai Zhang

A Class of topological nodal rings and its realization in carbon networks

Yan Gao[1], Yuanping Chen[1]*, Yuee Xie[1], Po-Yao Chang[2], Marvin L. Cohen[3], and Shengbai Zhang[4]

[1]*School of Physics and Optoelectronics, Xiangtan University, Xiangtan, 411105, Hunan, China*
[2]*Center for Materials Theory, Rutgers University, Piscataway, New Jersey, 08854, USA*
[3]*Department of Physics, University of California at Berkeley, and Materials Sciences Division, Lawrence Berkeley National Laboratory, Berkeley, California 94720, USA*
[4]*Department of Physics, Applied Physics, and Astronomy Rensselaer Polytechnic Institute, Troy, New York, 12180, USA*

Abstract

Topological nodal rings can be classified into three types according to the slopes in their energy dispersion. Type-I nodal rings consist of type-I points, type-II rings consist of type-II points, and type-III rings consist of anisotropic points. Taking carbon networks as an example, we show that all three types can exist and transform from one to another under experimentally realizable strain. Within a given type, a transition between a topological metal phase and a semiconductor phase also takes place, and each type of nodal rings shrinks into the corresponding type of semi-Dirac points, including novel type-II and III semi-Dirac points. These topological features are expected to exhibit diverse electron-hole pocket patterns and Landau levels, giving rise to unusual transport properties.

Corresponding author: chenyp@xtu.edu.cn

The study of topological semimetals/metals (TMs) are at the forefront of research in the materials and physical sciences[1-4]. With the discoveries of unusual band crossings near the Fermi level between two[5,6] or multiple bands[7-9], new topological concepts have emerged, such as the Dirac point[10,11], Weyl point[12,13], and nodal line[14-16]. Each new finding expands the class of topological systems, often with new physical properties. Therefore, searches for new classes of topological matter have been a recent focus[17,18].

Type II Weyl point[19,20] is a new topological feature, which is distinctly different from type I point[21,22] because of their qualitatively different band slopes. The conduction and valence bands of type-II points have the same sign of slopes, while those of type-I points must have opposite signs[23-25]. This violates the Lorentz invariance, which is required in high-energy physics, but unnecessary for condensed matter systems[26]. Type-I and II Weyl points share the same topological characteristics, but with drastically different Fermi surfaces which can transform from one to the other by a Lifshitz transition[27-29]. Since magnetic properties and carrier transport are sensitive to the geometry of the Fermi surface, they can be drastically different at type-I and type-II Weyl points as well[30,31].

The distinction between Weyl points hints that band dispersion near a topological gapless region can play a significant role in the various TMs to result in drastically different physical properties – an idea that, however, has not yet been explored in nodal-ring semimetal systems (NRSMs). Note that unlike the zero-dimensional Dirac or Weyl points, which are discrete points in the Brillouin zone (BZ), band crossing in NRSMs usually generates one-dimensional rings[32,33] with variously intriguing properties such as drumhead surface states[34,35], unexpectedly strong correlation[36], unique Landau levels (LLs)[37], and superconductivity[38]. To date, NRSMs have been predicted for carbon networks[39-45], hyper-honeycomb lattices[46], CaP_3[47], LaN[48], $ZrSiS$[49], $Cu_3(Pd,Zn)N$[32], in which most nodal rings are

made of only type-I nodal points. Question arises: do new classes of nodal rings exist in nature and what new physical properties can in principle be realized?

In this Letter, we provide the classification of nodal rings and, using carbon networks as an example, we demonstrate the complete classification to have three types. Type-I and II rings are made of two bands of opposite- and same-sign slopes (in the directions normal to the ring), respectively, and type-III ring is anisotropic, made of bands having the same-sign slope in one direction but opposite-sign slopes in the other (orthogonal) direction. These nodal rings exhibit a wide range of different electron and hole pockets (EHPs) to affect carrier transport and optical absorption, e.g., allowed optical absorptions in type-I and II NRSMs are mutually exclusive from each other. In both type-II and III NRSMs, it is also observed that spacings between the Landau levels can collapse to practically zero – a feature that has not been observed in type-I NRSM.

Our first-principles calculations were based on the density functional theory (DFT) within the PBE approximation[50] for the exchange-correlation energy. The core-valence interactions were described by the projector augmented-wave potentials[51], as implemented in the VASP code[52]. Plane waves with a kinetic energy cutoff of 600 eV were used as the basis set. The calculations were carried out in periodic supercells[53]. The atomic positions were optimized using the conjugate gradient method, in which the energy convergence criterion between two consecutive steps was set at 10^{-6} eV. The maximum allowed force on the atoms was 10^{-3} eV/Å.

Figures 1(a-b) show the atomic structures of two carbon networks (CNWs). Both are formed by connecting armchair nanoribbons of widths m and n shown in Fig. 1(c), named as CNW-(m,n). The variation of m and n produces a series of carbon networks. Figures 1(a) and 1(b) correspond to CNW-(3,2) and (1,2), respectively. At the connecting lines, the (gray) atoms are sp^3 hybridized; while the atoms in the nanoribbons (blue C_1 and pink C_2) are sp^2 hybridized. Figure 1(d) shows the conventional and primitive cells of CNW-(1,2).

The space groups of CNW-(3,2) and (1,2) are both IMMA with a mirror M_z normal to z. The calculated cohesive energies indicate that CNW-(3,2) (-7.67eV/C) and CNW-(1,2) (-7.47eV/C) are metastable carbon allotropes, as they are only 0.1-0.3 eV/C smaller than that of diamond. To assess the stability, we also calculated their phonon spectra, and did not find any soft-modes in the BZ. [See details in Table S1 and Fig. S1 in the Supplemental Material (SM)][54].

To model the band structure of CNW-(1,2) near the Fermi level, we note that its primitive cell, shown in the bottom panel of Fig. 1(d), contains 4 "pink" and 4 "blue" atoms. Each contributes one π orbital to the bands closest to the Fermi level. As will be shown later, only the 4 "pink" atoms contribute to the band dispersion near the Fermi level[55-57]. Therefore, a 4×4 TB model is sufficient to describe the band structure, which reads

$$H = \sum_{<i,j>} \sum_{\mu} t_{ij} e^{-ik \cdot d_{ij}^{\mu}}, \tag{1}$$

where i, j label the four C_2 atoms, d_{ij}^{μ} is the distance vector directed from atom j to atom i, t_{ij} is the hopping energy between π ($p_\perp$) orbitals of the atoms, and μ runs over all equivalent lattice sites. For t_{ij}, we consider five parameters: the intra-ribbon interactions t_1 and t_2, and inter-ribbon interactions t_3, t_4, and t_5[Figs. 1(c-d)]. As it turns out, the same Hamiltonian also works for CNW-(3,2), which has the same space group as CNW-(1,2) and whose primitive cell also contains 4 "pink" atoms.

Our calculations indicate that t_3, t_4 and t_5 have a significant effect on the band structure whose dispersion can be classified into three types, type-I, II and III (as detailed in Fig. S2, SM)[54]. Depending on t_1, each type of band structures experiences a phase transition from a

topological NRSM to a semiconductor and, at the transition, the system exhibits a characteristic semi-Dirac point (SDP). Figures 2(a-c) show schematically the three types of SDPs where the contacting bands are all linear along k_z, but all quadratic along k_x and k_y. The differences among the three types are the slope signs of the quadratic bands. Type-I in Fig. 2(a) is a standard SDP[58-60], where the quadratic conduction and valence bands have slopes of opposite signs at the crossing. Type-II and III in Figs. 2(b-c) are two new types of SDPs: in type-II, the quadratic valence band has the same slope sign as the quadratic conduction band; in type-III, however, the slope sign is the same along k_x but opposite along k_y. These, combined with the fact that along k_z the dispersion is linear, suggest that type-III SDP has the most pronounced anisotropy among all three types.

Further change of t_1 leads to a crossing between the valance and conduction bands. As a result, the SDPs evolve into three types of nodal rings [Figs. S2(g-i), SM][54]. The band structures at $k_z = 0$ of the three types of rings are schematically shown in Figs. 2(d-f), where both the type-I and II rings may be viewed as crossing lines between two paraboloids [i.e., the green lines in Figs. 2(d-e)]. The paraboloids open in the opposition direction along E in type-I rings, but in same direction in type-II rings, in accordance with the definitions of type-I and II Dirac points. On the other hand, a type-III ring is defined by the crossing between a paraboloid and a saddle surface, as shown in Fig. 2(f), where the Dirac points are type-I along k_y but type-II along k_x. In other words, each point is anisotropic.

The three types of rings, and associated phase transitions, are all reproduced by DFT calculations. Figure 3(a) shows the PBE band structure of CNW-(3,2). There are type-I Dirac points near the Fermi level along Γ-X, Γ-S and Γ-Y directions, which are representative of type-I rings [i.e., the green circle in the inset of Fig. 3(a)] in the $k_z = 0$ plane. In the TB model, the ring evolves with t_1 (describing hopping along z), whose effects may be mimicked by an external

strain also along z in the DFT. When a compressive +2.3% strain is applied, the ring shrinks into a type-I SDP at Γ [Fig. 3(b)]. At a higher strain, a band gap appears, in qualitative agreement with the TB model.

Figure 3(c) shows the band structure of CNW-(1,2), which is metallic. There exist two (red) bands which are linear along k_z (i.e., Γ-Z) but quadratic otherwise. The quadratic bands have the same slope sign along k_x (Γ-X) but opposite slope signs along k_y (Γ-Y). At E = -0.28 eV, the two bands touch each other at Γ, giving rise to a SDP. The band structure in the inset of Fig. 3(c) qualitatively agrees with the type-III SDP of the TB model in Fig. 2(c). When a compressive +2.2% strain is applied along z, the two bands cross to generate several Dirac points [Fig. 3(d)], e.g., one type-II point along k_x and one type-I point along k_y, which are representative of the type-III ring in the inset of Fig. 3(d). When a tensile strain is applied along z, the system becomes a semiconductor. On the other hand, type-II ring can be realized in CNW-(1,2) by applying a strain along x (Fig. S3, SM)[54]. The DFT band structures in Fig. 3 are projected onto atomic orbitals, revealing that all the bands near the Fermi level originate from π orbitals of the C_2 atoms. These results are consistent with the charge density plot in the inset of Fig. 3(b). Therefore, the use of Eq. (1), based on π orbitals to describe the near-Fermi-level states for CNW-(3,2) and (1,2), is justified.

Note that our discussion has so far been centered on the CNWs for their similarity with realistic systems. However, the classification of new types of nodal rings, which is the central point of this paper, needs not be limited to any specific systems. For this purpose, the TB model in Eq. (1) is no longer necessary, since the classification only requires the knowledge of the curvature of the energy bands, which can be straightforwardly obtained by a k•p model at Γ up to k-quadratic terms:

$$H(k) = \begin{bmatrix} A_1 k_x^2 + B_1 k_y^2 & iCk_z \\ -iCk_z & \Delta + A_2 k_x^2 + B_2 k_y^2 \end{bmatrix},$$ (2)

where Δ is the gap, and A_1, B_1, A_2, B_2 and C are band parameters obtained by fitting DFT results.

By changing the signs of A_1, B_1, A_2 and B_2, three types of nodal rings including 6 irreducible subtypes are listed in Table I. Type-I, II and III nodal rings mentioned above belong to them. Note that the subtype-3 nodal ring in type II is a crossing line of two saddle surfaces(Fig. S4(a) in SM)[54]. It is an anisotropic type-II ring because of inverse band slopes along k_x and k_y, which has not been reported in the former literatures.

These nodal rings, sharing the same topological characteristic, are protected by the mirror symmetry M_z normal to z. The protection can also be inferred from the 1D winding number:

$N = \frac{1}{\pi} \oint_l A_k \cdot dk$ where A_k is the Berry connection at point k[61]. Our calculation shows that N

$= \pm 1$, which is effectively the same for all the rings.

One of the consequences of the nodal rings is the formation of EHPs[62,63], which are highlighted by orange for hole pockets and light blue for electron pockets. Figures 4(a-c) show the projections of the rings as green dashed lines, as well as the Fermi surfaces as the borderlines of the colored pockets. At the four yellow crossing points, the rings intersect the Fermi surfaces. Note that, for type-I and II rings, the Fermi surfaces may be described by two equi-energy ellipses centered at the origin but with different long axes: one along k_x and the other along k_y. The EHPs of type-I rings reside in the (tiny) non-overlapping regions between the two ellipses, whereas those of type-II rings complement exactly the EHPs of type-I rings to occupy the remaining (large) regions. As such, if the ellipses in Figs. 4(a-b) were circles, type-I EHPs would completely disappear while type-II EHPs would occupy the whole plane in the figure. The EHPs

of type-III rings, on the other hand, are mostly anisotropic with the electron pockets residing in the fan-shaped regions near the center, whereas the hole pockets reside in the approximate trapezoids on the peripherals. Also, type-III rings cannot have fixed energies. As a result, under no circumstance, the EHPs for type-III rings will vanish.

The rich Fermi surface morphologies and EHP patterns, associated with the three types of nodal rings, suggest that these systems may exhibit a variety of interesting physical properties[64,65]. Consider, for example, carrier transport through scattering by phonons of small q: in a type-I ring, transport along y should be dominated by electrons but along x by holes; in a type-II ring, in contrast, transport should be dominated by inter-EHP scatterings; in a type-III ring, on the other hand, transport involves only states near Γ and the four (yellow) vertices in Fig. 4(c), and should hence be highly anisotropic. These qualitative differences can help experimental determination of the type of nodal rings.

Another noticeable difference of the three types of rings is their LLs, shown in Figs. 4(d-f). Here, an external B field along z is applied by replacing k_x and k_y in Eq. (2) with $k_x - eA_x$ and $k_y - eA_y$, respectively, where $\boldsymbol{A} = (-By/2, Bx/2)$. The LLs are obtained by solving Eq. (2)[66] using, for simplicity, the parameters in Table 1. For a type-I ring, we have

$$E_{\pm}^{n} = \frac{1}{2}\Delta \pm \frac{1}{2}\sqrt{\Delta^2 + 4[k_z^2 + E_n(E_n - \Delta)]}, \tag{3}$$

where $E_n = eB(2n + 1)$. At $k_z = 0$, we have $E_{+}^{n} = \Delta - E_n$ and $E_{-}^{n} = E_n$ [Fig. 4(d)]. The LL spacing, given by $\left|E_{\pm}^{n} - E_{\pm}^{n-1}\right|$, in this case is a constant $2eB$. For a type-II ring, we have instead

$$E_{\pm}^{n} = \frac{1}{2}[E_n(1 + \gamma) + \Delta] \pm \frac{1}{2}\sqrt{[E_n(1 + \gamma) + \Delta]^2 + 4[k_z^2 - E_n(\gamma E_n + \Delta)]}. \tag{4}$$

At $k_z = 0$, $E_{+}^{n} = \Delta + \gamma E_n$ and $E_{-}^{n} = E_n$, shown in Fig. 4(e) for a typical value of $\gamma = 0.5$. Here,

the LL spacing is given by $2\gamma eB$ $(0 \leq \gamma < 1)$, which vanishes in the extreme case when $\gamma = 0$.

For a type-III ring, no simple analytic solution exists. Instead, we apply second-order perturbation theory to obtain, at $k_z = 0$, $E_+^n = \Delta + \frac{1}{8} E_n[(\delta + 3)^2 - 12]$ and $E_-^n = E_n$, shown in

Fig. 4(f) for a typical value of $\delta = 0.5$. The LL spacing is a constant for the E_-^n branch (similar to type-I and II rings) but varies for the E_+^n branch. When $\delta \approx 0.46$, all E_+^n values become equal. Hence, type-III ring can be a degenerate Landau metal.

The three types of nodal rings are also expected to exhibit diverse optical properties. From Figs. 2(d-f), we see that if optical absorption in a type-I ring is large, it must be small in a type-II ring because the two are mutually exclusive. For a type-III ring, strong absorption can only take place in the k-direction where the slope signs of the bands are opposite. Other emerging phenomena such as superconductivity, CDW, and nesting instabilities have also been suggested for type-I rings[67-70], and may be more interesting in type-II and III rings.

In summary, a theory that classifies topological nodal rings into three types with diverse physical properties is developed. Among the rings, type-III may deserve the most attention for its maximum anisotropy. The EHPs of the rings exhibit a rich variety of patterns, which can serve as a platform to study fundamental electronic and magnetic properties of the rings such as anisotropy in electron/hole transport and collapse of LLs. It is known that nodal rings are subject to (Lifshitz) phase transition, through which the EHPs gradually evolve from one to the other – a phenomenon that may be used to study electron-hole friction and strongly-correlated Coulomb interaction in the flat-band region at the transition. Our work is not solely based on a toy model, but is centered on carbon networks of reasonable stabilities. The recent interest in such systems raises the hope that soon the different types of nodal rings may be experimentally realized.

References

[1]   A. A. Burkov, Nat. Mater. **15**, 1145 (2016).

[2]   Z. Liu, B. Zhou, Y. Zhang, Z. Wang, H. Weng, D. Prabhakaran, S.-K. Mo, Z. Shen, Z. Fang, and X. Dai, Science **343**, 864 (2014).

[3]   B. Q. Lv, N. Xu, H. M. Weng, J. Z. Ma, P. Richard, X. C. Huang, L. X. Zhao, G. F. Chen, C. E. Matt, F. Bisti, V. N. Strocov, J. Mesot, Z. Fang, X. Dai, T. Qian, M. Shi, and H. Ding, Nat. Phys. **11**, 724 (2015).

[4]   T. Bzdusek, Q. Wu, A. Ruegg, M. Sigrist, and A. A. Soluyanov, Nature **538**, 75 (2016).

[5]   A. H. Castro Neto, N. M. R. Peres, K. S. Novoselov, and A. K. Geim, Rev. Mod. Phys. **81**, 109 (2009).

[6]   S. M. Young and C. L. Kane, Phys. Rev. Lett. **115**, 126803 (2015).

[7]   Z. Zhu, G. W. Winkler, Q. Wu, J. Li, and A. A. Soluyanov, Phys. Rev. X **6**, 031003 (2016).

[8]   B. J. Wieder, Y. Kim, A. M. Rappe, and C. L. Kane, Phys. Rev. Lett. **116**, 186402 (2016).

[9]   B. Bradlyn, J. Cano, Z. Wang, M. G. Vergniory, C. Felser, R. J. Cava, and B. A. Bernevig, Science **353**, aaf5037 (2016).

[10]   J. A. Steinberg, S. M. Young, S. Zaheer, C. L. Kane, E. J. Mele, and A. M. Rappe, Phys. Rev. Lett. **112**, 036403 (2014).

[11]   H. Li, H. He, H. Z. Lu, H. Zhang, H. Liu, R. Ma, Z. Fan, S. Q. Shen, and J. Wang, Nat. Commun. **7**, 10301 (2016).

[12]   B. Q. Lv, H. M. Weng, B. B. Fu, X. P. Wang, H. Miao, J. Ma, P. Richard, X. C. Huang, L. X. Zhao, G. F. Chen, Z. Fang, X. Dai, T. Qian, and H. Ding, Phys. Rev. X **5**, 031013 (2015).

[13]   L. Lu, Z. Wang, D. Ye, L. Ran, L. Fu, J. D. Joannopoulos, and M. Soljačić, Science **349**, 622 (2015).

[14]   A. A. Burkov, M. D. Hook, and L. Balents, Phys. Rev. B **84**, 235126 (2011).

[15]   R. Li, H. Ma, X. Cheng, S. Wang, D. Li, Z. Zhang, Y. Li, and X. Q. Chen, Phys. Rev. Lett. **117**, 096401 (2016).

[16]   Y. Kim, B. J. Wieder, C. L. Kane, and A. M. Rappe, Phys. Rev. Lett. **115**, 036806 (2015).

[17]   J. Jiang, Z. Liu, Y. Sun, H. Yang, C. Rajamathi, Y. Qi, L. Yang, C. Chen, H. Peng, and C. Hwang, Nat. Commun. **8**, 13973 (2017).

[18]   G. Autes, D. Gresch, M. Troyer, A. A. Soluyanov, and O. V. Yazyev, Phys. Rev. Lett. **117**, 066402 (2016).

[19]   A. A. Soluyanov, D. Gresch, Z. Wang, Q. Wu, M. Troyer, X. Dai, and B. A. Bernevig, Nature **527**, 495 (2015).

[20]   Z. Wang, D. Gresch, A. A. Soluyanov, W. Xie, S. Kushwaha, X. Dai, M. Troyer, R. J. Cava, and B. A. Bernevig, Phys. Rev. Lett. **117**, 056805 (2016).

[21]   S.-Y. Xu, N. Alidoust, I. Belopolski, Z. Yuan, G. Bian, T.-R. Chang, H. Zheng, V. N. Strocov, D. S. Sanchez, G. Chang, C. Zhang, D. Mou, Y. Wu, L. Huang, C.-C. Lee, S.-M. Huang, B. Wang, A. Bansil, H.-T. Jeng, T. Neupert, A. Kaminski, H. Lin, S. Jia, and M. Zahid Hasan, Nat. Phys. **11**, 748 (2015).

[22]   S. M. Huang, S. Y. Xu, I. Belopolski, C. C. Lee, G. Chang, B. Wang, N. Alidoust, G. Bian, M. Neupane, C. Zhang, S. Jia, A. Bansil, H. Lin, and M. Z. Hasan, Nat Commun **6**, 7373 (2015).

[23]   Y. Xu, F. Zhang, and C. Zhang, Phys. Rev. Lett. **115**, 265304 (2015).

[24]   K. Koepernik, D. Kasinathan, D. Efremov, S. Khim, S. Borisenko, B. Büchner, and J. van den Brink, Phys. Rev. B **93**, 201101 (2016).

[25]   G. Chang, S.-Y. Xu, D. S. Sanchez, S.-M. Huang, C.-C. Lee, T.-R. Chang, G. Bian, H. Zheng, I. Belopolski, and N. Alidoust, Sci. Adv. **2**, e1600295 (2016).

[26]   D. S. Sanchez, S. Y. Xu, N. Alidoust, G. Chang, H. Lu, B. Singh, I. Belopolski, X. Zhang, G. Bian, and H. Zheng, Sci. Adv. **3**, e1603266 (2017).

[27]   G. E. Volovik, Low Temp. Phys. **43**, 47 (2017).

[28]   H. Huang, S. Zhou, and W. Duan, Phys. Rev. B **94**, 121117 (2016).

[29]   A. Cortijo, D. Kharzeev, K. Landsteiner, and M. A. H. Vozmediano, Phys. Rev. B **94**, 241405 (2016).

[30]   A. Tamai, Q. Wu, I. Cucchi, F. Y. Bruno, S. Riccò, T. Kim, M. Hoesch, C. Barreteau, E. Giannini, and C. Besnard, Phys. Rev. X **6**, 031021 (2016).

[31]   Z.-M. Yu, Y. Yao, and S. A. Yang, Phys. Rev. Lett. **117**, 077202 (2016).

[32]   R. Yu, H. Weng, Z. Fang, X. Dai, and X. Hu, Phys. Rev. Lett. **115**, 036807 (2015).

[33]   L.-K. Lim and R. Moessner, Phys. Rev. Lett. **118**, 016401 (2017).

[34]   G. Bian, T.-R. Chang, H. Zheng, S. Velury, S.-Y. Xu, T. Neupert, C.-K. Chiu, S.-M. Huang, D. S. Sanchez, and I. Belopolski, Phys. Rev. B **93**, 121113 (2016).

[35]   Y.-H. Chan, C.-K. Chiu, M. Chou, and A. P. Schnyder, Phys. Rev. B **93**, 205132 (2016).

[36]   Y. Huh, E.-G. Moon, and Y. B. Kim, Phys. Rev. B **93**, 035138 (2016).

[37]   J.-W. Rhim and Y. B. Kim, Phys. Rev. B **92**, 045126 (2015).

[38]   G. Bian, T.-R. Chang, R. Sankar, S.-Y. Xu, H. Zheng, T. Neupert, C.-K. Chiu, S.-M. Huang, G. Chang, and I. Belopolski, arXiv preprint arXiv:1505.03069 (2015).

[39]   J. T. Wang, H. Weng, S. Nie, Z. Fang, Y. Kawazoe, and C. Chen, Phys. Rev. Lett. **116**, 195501 (2016).

[40]   H. Weng, Y. Liang, Q. Xu, R. Yu, Z. Fang, X. Dai, and Y. Kawazoe, Phys. Rev. B **92**, 045108 (2015).

[41]   Y. Cheng, X. Feng, X. Cao, B. Wen, Q. Wang, Y. Kawazoe, and P. Jena, Small **13**, 1602894 (2017).

[42]   Z. Zhu and D. Tománek, Phys. Rev. Lett. **109**, 135501 (2012).

[43]   Z. Zhu, Z. G. Fthenakis, J. Guan, and D. Tománek, Phys. Rev. Lett. **112**, 026803 (2014).

[44]   C. Zhong, Y. Chen, Y. Xie, S. A. Yang, M. L. Cohen, and S. B. Zhang, Nanoscale **8**, 7232 (2016).

[45]   Y. Chen, Y. Xie, S. A. Yang, H. Pan, F. Zhang, M. L. Cohen, and S. Zhang, Nano Lett. **15**, 6974 (2015).

[46]   K. Mullen, B. Uchoa, and D. T. Glatzhofer, Phys. Rev. Lett. **115**, 026403 (2015).

[47]   Q. Xu, R. Yu, Z. Fang, X. Dai, and H. Weng, Phys. Rev. B **95**, 045136 (2017).

[48]   M. Zeng, C. Fang, G. Chang, Y.-A. Chen, T. Hsieh, A. Bansil, H. Lin, and L. Fu, arXiv preprint arXiv:1504.03492 (2015).

[49]   L. M. Schoop, M. N. Ali, C. Straßer, A. Topp, A. Varykhalov, D. Marchenko, V. Duppel, S. S. Parkin, B. V. Lotsch, and C. R. Ast, Nat. Commun. **7**, 11696 (2016).

[50]   P. JP, B. K, and E. M, Phys. Rev. Lett. **77**, 3865 (1996).

[51]   G. Kresse and D. Joubert, Phys. Rev. B **59**, 1758 (1999).

[52]   G. Kresse and J. Furthmüller, Comput. Mater. Sci. **6**, 15 (1996).

[53]   M. L. Cohen, M. Schlüter, J. R. Chelikowsky, and S. G. Louie, Phys. Rev. B **12**, 5575 (1975).

[54]   See Supplemental Material at [URL will be inserted by publisher] for phonon dispersion results, tight-binding band structure of type-I,type-II and type-III nodal rings, band structure of CNW-(1,2) under a strain, subtype-3 in type-II topological nodal ring and crystal structure information.

[55]   V. Meunier, A. Souza Filho, E. Barros, and M. Dresselhaus, Rev. Mod. Phys. **88**, 025005 (2016).

[56]   L. Yang, C.-H. Park, Y.-W. Son, M. L. Cohen, and S. G. Louie, Phys. Rev. Lett. **99**, 186801 (2007).

[57]   Y.-W. Son, M. L. Cohen, and S. G. Louie, Phys. Rev. Lett. **97**, 216803 (2006).

[58]   C. Zhong, Y. Chen, Y. Xie, Y. Y. Sun, and S. Zhang, Phys. Chem. Chem. Phys. **19**, 3820 (2017).

[59]   V. Pardo and W. E. Pickett, Phys. Rev. Lett. **102**, 166803 (2009).

[60]   S. Banerjee, R. Singh, V. Pardo, and W. Pickett, Phys. Rev. Lett. **103**, 016402 (2009).

[61]   G. Bian, T.-R. Chang, R. Sankar, S.-Y. Xu, H. Zheng, T. Neupert, C.-K. Chiu, S.-M. Huang, G. Chang, and I. Belopolski, Nat. Commun. **7**, 10556 (2016).

[62]   R. Yu, Q. Wu, Z. Fang, and H. Weng, Phys. Rev. Lett. **119**, 036401 (2017).

[63]   E. Emmanouilidou, B. Shen, X. Deng, T.-R. Chang, A. Shi, G. Kotliar, S.-Y. Xu, and N. Ni, Phys. Rev. B **95**, 245113 (2017).

[64]   S. Zhong, J. E. Moore, and I. Souza, Phys. Rev. Lett. **116**, 077201 (2016).

[65]   P. K. Das, D. Di Sante, I. Vobornik, J. Fujii, T. Okuda, E. Bruyer, A. Gyenis, B. Feldman, J. Tao, and R. Ciancio, Nat. Commun. **7**, 10847 (2016).

[66]   D. Tong, arXiv preprint arXiv:1606.06687 (2016).

[67]   S. Li, Z.-M. Yu, Y. Liu, S. Guan, S.-S. Wang, X. Zhang, Y. Yao, and S. A. Yang, Phys. Rev. B **96**, 081106 (2017).

[68]   I. Mazin, D. J. Singh, M. Johannes, and M.-H. Du, Phys. Rev. Lett. **101**, 057003 (2008).

[69]   D. LeBoeuf, N. Doiron-Leyraud, J. Levallois, R. Daou, J.-B. Bonnemaison, N. Hussey, L. Balicas, B. Ramshaw, R. Liang, and D. Bonn, Nature **450**, 533 (2007).

[70]   T. Kidd, T. Miller, M. Chou, and T.-C. Chiang, Phys. Rev. Lett. **88**, 226402 (2002).
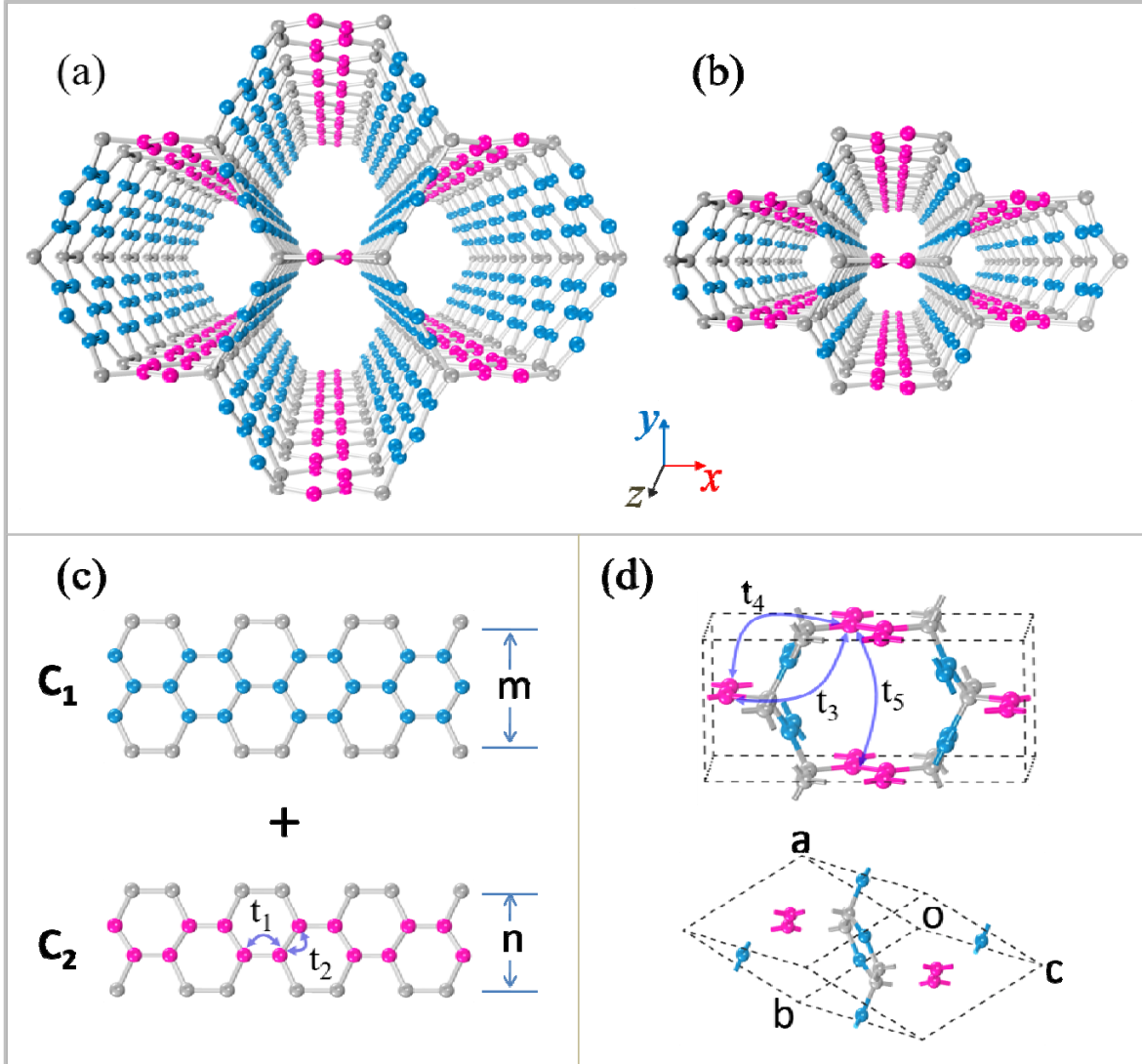
Figure 1. (Color online) Atomic structures of (a) CNW-(3,2) and (b) CNW-(1,2), in which the common $n = 2$ pink nanoribbons run along z. They belong to the same series of CNW-(m,n), formed by connecting the armchair ribbons in (c) of width m and n. Both blue C_1 and pink C_2 balls are sp^2 atoms, while gray balls are sp^3 atoms. (d) (Top) Conventional and (bottom) primitive cells of CNW-(1,2). Symbols t_1, t_2 in (c) and t_3, t_4 and t_5 in (d) denote hopping parameters.
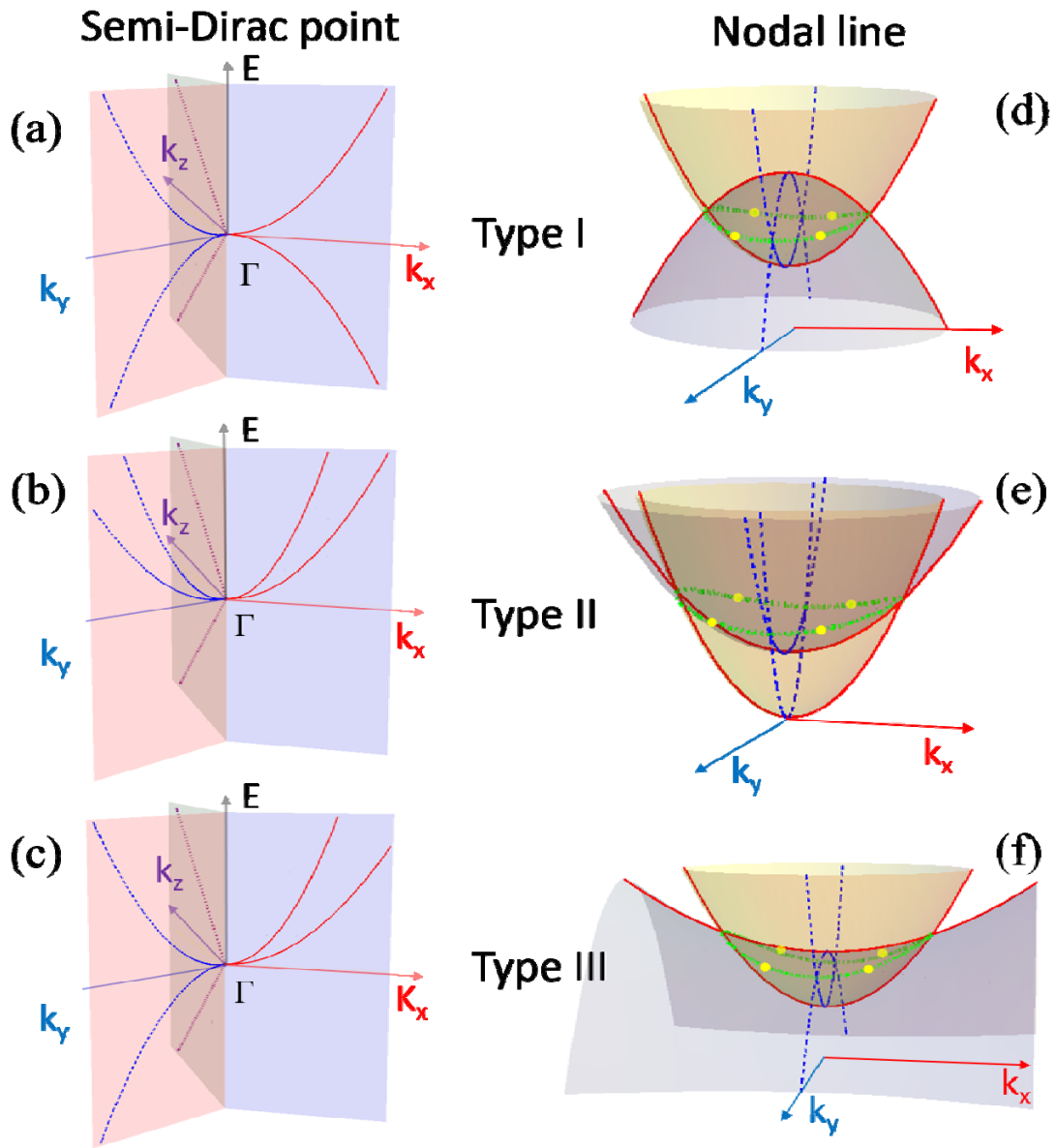
Figure 2. (Color online) Three types of SDPs and nodal rings. (a-c) Type-I, II, and III SDPs. The red (solid), blue (dashed) and olive (dotted) lines denote the energy bands along k_x, k_y and k_z, respectively. (d-f) Type-I, II, and III topological nodal rings at $k_z = 0$. They are shown as green (dotted) circles, which intersect the (equi-energy) Fermi level at the four yellow points.
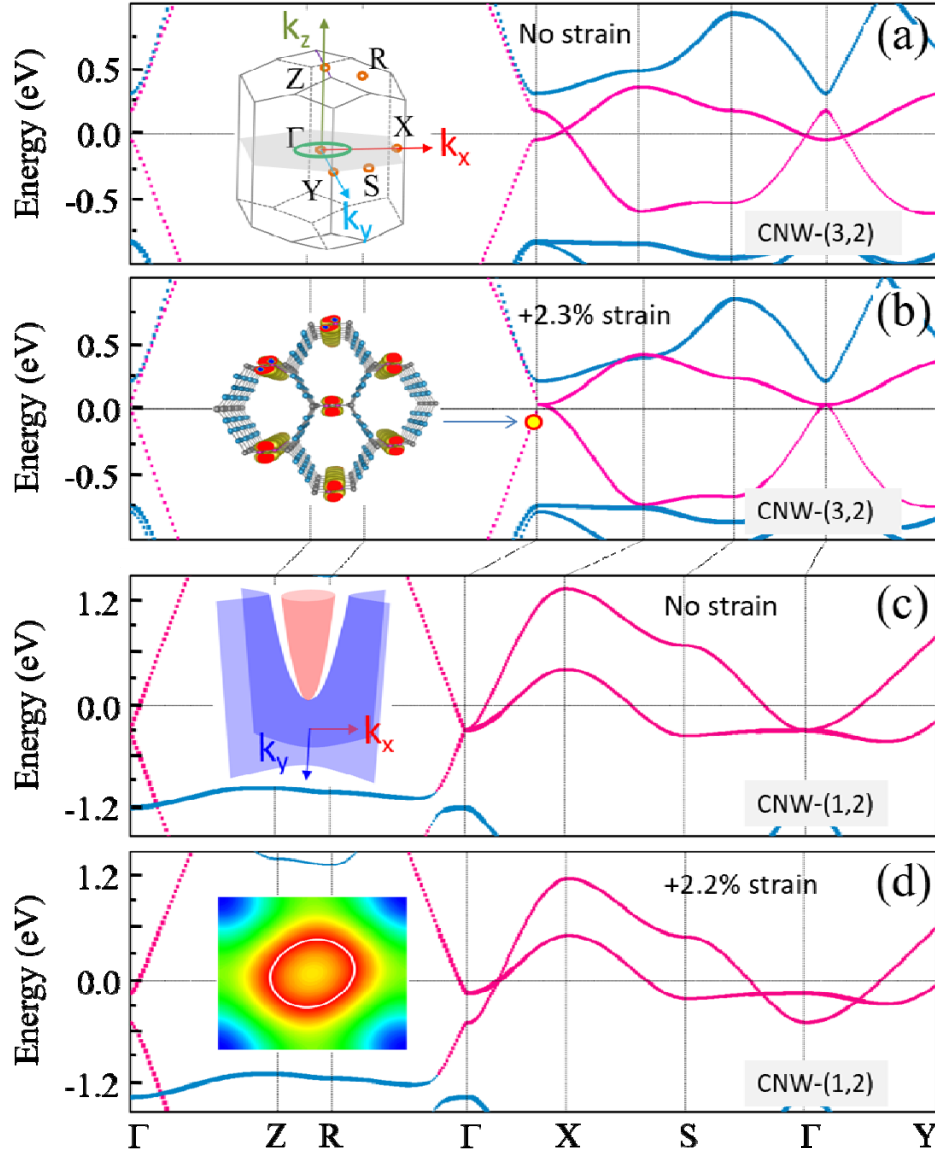
Figure 3. (Color online) Band structure projected onto atomic orbitals: pink corresponds to C_2 $p_\perp$ orbitals and blue corresponds to C_1 $p_{\parallel/\perp}$ orbitals. (a-b) CNW-(3,2): (a) under no strain. Inset is the first BZ, where the green circle denotes the location of the type-I nodal ring. (b) Under a compressive +2.3% strain along z. Inset is the charge density plot for states near the type-I SDP. (c-d) CNW-(1,2): (c) under no strain. Inset is a band structure near the type-III SDP. (d) Under a compressive +2.2% strain along z. Inset is a contour plot of type-III ring at $k_z = 0$.
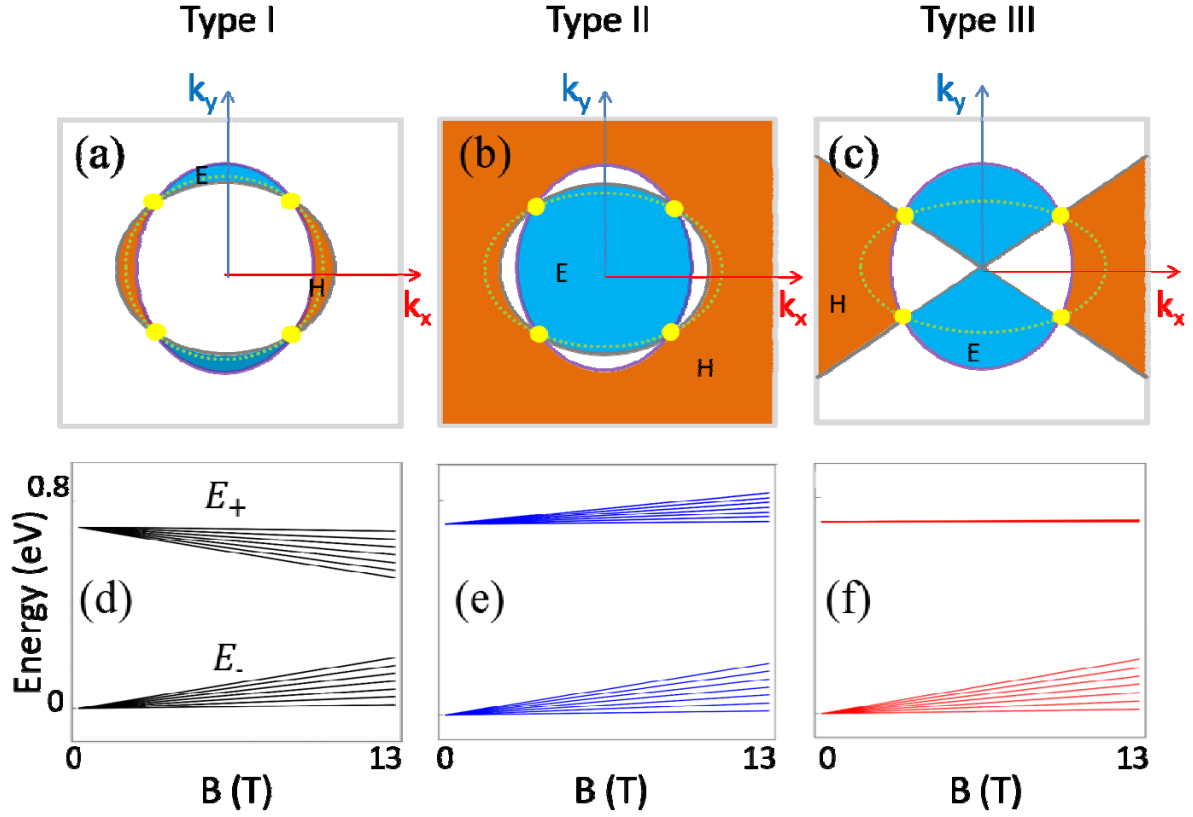
Figure 4. (Color online) (a-c) EHPs for type-I, II, and III nodal rings. Light blue and orange colors denote electron (E) and hole (H) pockets, respectively. Green dotted circles and yellow points have the same meanings as in Figs. 2(d-f). (d-f) LLs for type-I, II (γ=0.5), and III (δ=0.5) nodal rings as a function of magnetic field B. In the calculation, we set k_z = 0 and Δ = 0.7 eV.

Table 1. Signs of parameters A_1, B_1, A_2 and B_2 in Eq. (2) for the three types of nodal rings. Note that a combination of different signs can generate a total of 16 subtypes: 4 belong to type-I, 4 belong to type-II and 8 belong to type-III nodal rings. After considering the similarity of these subtypes, type-I, II and III nodal rings have 1, 3 and 2 irreducible subtypes, respectively, and their signs are listed. The figure in the parentheses in the subtype column represents the number of similar subtypes. The first subtypes of the type I, II and III nodal rings respectively correspond to the cases in Figs. 2(d-f). Last column gives parameters (in unit of $10/m_0$ where m_0 is the free electron mass) to simplify the model in Eq. (2) for representative LL calculations.

Type	Subtype	A_1	B_1	A_2	B_2	Simplified model ($C = 1$, $\Delta = 0$)
I	1 (4)	+	+	-	-	$A_1 = B_1 = -A_2 = -B_2 = 1$
II	1	+	+	+	+	$A_1 = B_1 = 1$, $A_2 = B_2 = \gamma$ $(0 \leq \gamma < 1)$
II	2	-	-	-	-	
II	3 (2)	+	-	+	-	
III	1 (4)	+	+	+	-	$A_1 = B_1 = -B_2 = 1$, $A_2 = \delta$ $(0 \leq \delta < 1)$
III	2 (4)	+	-	-	-	